Eur. Phys. J. B **59**, 509–518 (2007)
DOI: 10.1140/epjb/e2007-00307-0

THE EUROPEAN PHYSICAL JOURNAL B

Transition to chaos via the quasi-periodicity and characterization of attractors in confined Bénard-Marangoni convection

S. Rahal[1,a], P. Cerisier[2,b], and C. Abid[2,c]

[1] Department of Mechanical Engineering, University of Batna, Rue Boukhlouf Mohamed el Hadi, 05000 Batna, Algeria
[2] IUSTI - CNRS UMR 6595, Polytech'Marseille, Technopôle de Château-Gombert, 5 rue Enrico Fermi, 13453, Marseille, France

Received 19 February 2007 / Received in final form 25 September 2007
Published online 15 November 2007 –

Abstract. A study of dynamic regimes in Bénard-Marangoni convection was carried out for various Prandtl and Marangoni numbers in small aspect ratio geometries ($\Gamma = 2.2$ and 2.8). Experiments in a small hexagonal vessel, for a large range of the Marangoni number (from 148 to 3636), were carried out. Fourier spectra and an auto-correlation function were used to recognize the various dynamic regimes. For given values of the Prandtl number ($Pr = 440$) and aspect ratio ($\Gamma = 2.2$), mono-periodic, bi-periodic and chaotic states were successively observed as the Marangoni number was increased. The correlation dimensions of strange attractors corresponding to the chaotic regimes were calculated. The dimensions were found to be larger than those obtained by other authors for Rayleigh-Bénard convection in aspect ratio geometries of the same order. The transition from temporal chaos to spatio-temporal chaos was also observed. For $\Gamma = 2.2$, when larger values of the Marangoni number were imposed ($Ma = 1581$ for $Pr = 160$ and $Ma = 740$ for $Pr = 440$), spatial modes were involved through the convective pattern dynamics.

PACS. 47.10.Fg Dynamic system methods – 47.52.+j Chaos in fluid dynamics

1 Introduction

In hydrodynamic instabilities, chaotic states are often observed. For example, in convection instabilities, for a given convective pattern and a fixed value of the Rayleigh number, a well-defined dynamic regime is observed. If the dynamics are chaotic, the observed chaos is temporal in a system for which spatial order is preserved. However, when the spatial modes are involved through the mobility of the pattern, spatio-temporal chaos is observed, which is characterized by the interaction between spatial and temporal modes leading to a dynamic disorder of the convective pattern.

Temporal chaos in confined geometries has been observed in surface waves, Rayleigh-Bénard (RB) convection and in other hydrodynamic instabilities [1–5]. Secondary instabilities and chaotic behaviours in extended geometries have also been studied theoretically and experimentally [1–3,6,7]. Indeed, transition to spatio-temporal chaos has been observed and characterized in various extended systems, such as Rayleigh-Bénard convection, optical instabilities, flames, chemical reactions, Faraday waves, a rotating convective system, etc... [1–3,7]. When such complex systems are studied, the most appropriate methods must be chosen to analyse their behaviour. Deterministic methods are often used for the characterization of confined systems and statistical tools for the study of extended geometries.

The study of Malkus [8] is among the first works devoted to time-dependent flows and turbulence in thermal convection. Subsequently, other authors observed irregular temperature fluctuations in convection and transitions to chaos or turbulence which were studied as a function of the Rayleigh number for various Prandtl numbers [9–11]. Rayleigh-Bénard (RB) convection has been extensively studied because it is the simplest example of a hydrodynamic system transiting to chaos [2]. Various experiments have been conducted in order to explore the possible scenarios of transition to chaos in RB convection including subharmonic cascade, intermittency and quasi-periodicity [12–19]. All these scenarios of transition go through the destabilization of a mono-periodic regime. In RB chaotic regimes it has also been found that the corresponding attractor dimensions are small in confined systems [20] and rather large in extended geometries [21].

The case of small aspect ratio geometries is particularly interesting to study because the confinement restricts the spectrum of spatial modes, which are allowed in extended geometries, to one or few competing modes.

[a] e-mail: samir.rahal@lycos.com
[b] e-mail: Pierre.Cerisier@polytech.univ-mrs.fr
[c] e-mail: cherifa.abid@polytech.univ-mrs.fr

Temporal and spatial modes can then be dissociated, thus allowing the study of the dynamic behaviour of the system. As mentioned above, such a study has been performed for RB instability. For Bénard-Marangoni (BM) convection (i.e. a horizontal fluid layer heated from below and cooled from above with a free upper surface), few works have been devoted to small vessels. These works have mainly been directed to the study of the onset of convection, the description of convective patterns and the conditions of the appearance of time-dependent flows [3]. More recently, a numerical study has been carried out on the transition to chaos for a fluid with a Prandtl number taken equal to zero [22].

As far as we know dynamic regimes occurring in confined BM convection have not been characterized using tools such as spectral methods and attractors. It is interesting to conduct such a study because in comparison with RB convection, for which buoyancy is the only effect involved, in studying a BM system both the buoyancy and the free surface tension effects have to be taken into account.

Thus, the aim of this work is to recognize the different dynamic regimes which appear when the vertical temperature difference is increased (Marangoni number rising), using spectral methods and measuring the degree of strangeness of chaotic regimes by their correlation dimensions. The observed dynamic regimes will be linked to the corresponding spatial modes by taking photographs of the convective patterns.

BM convection is governed mainly by the following dimensionless numbers: the Marangoni number: $Ma = (-d\sigma/dT)\ (\Delta T d/\rho\nu\chi)$ where σ is the surface tension, ΔT the vertical difference of temperature between the horizontal limiting surfaces, d the depth of the oil layer, ρ the density of the oil, ν its kinematic viscosity and χ the thermal diffusivity, the Rayleigh number: $Ra = \alpha g \Delta T d^3/\nu\chi$, where α is the expansion coefficient of the silicone oil and g the acceleration due to gravity, the Prandtl number $Pr = \nu/\chi$; the aspect ratio $\Gamma = A^{1/2}/d$, where A is the area of the oil layer free surface in the hexagonal vessel for our experimental set-up.

The influence of the above-mentioned physical parameters (Marangoni number, *Ma*, from 148 to 3636), Prandtl number ($Pr = 160$ or 440) and the aspect ratio ($\Gamma = 2.2$ or 2.8) was considered. The outline of this paper is the following: experimental procedure and data processing techniques are described in Section 2; in Section 3, the analysis methods are briefly described; typical experimental results are given in Section 4; finally, some conclusions are given in Section 5.

2 Experimental procedure and data processing techniques

2.1 Experimental procedure

The experimental principle used to conduct this study was to link the dynamic regimes observed to a physical parameter that could be measured non-intrusively and which accurately reflected the dynamic behaviour of the system. The use of horizontal laser beam deflection in [23,24] allowed the recognition of the dynamic regimes and the various scenarios of transition to chaos in RB convection, for which the deflection is due only to buoyancy and to the corresponding temperature gradients within the liquid layer.

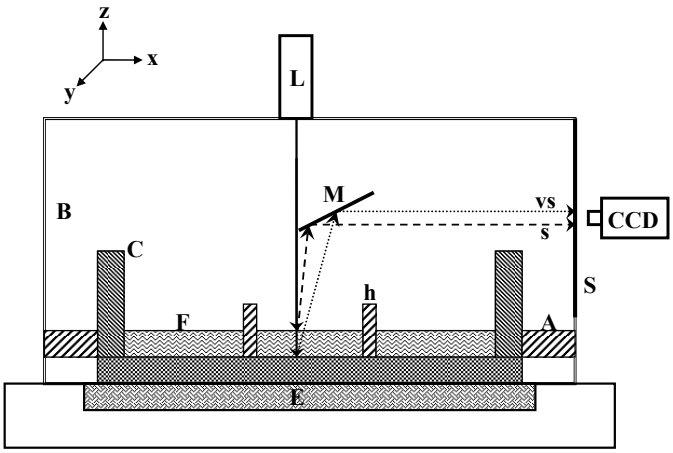

Fig. 1. Experimental set-up. C: Circular container, h: Hexagonal vessel, F: Fluid, M: Mirror, L: Laser, S: Screen, CCD: Camera, B: Box, A: Annular insulating plate, E: Electric heater (Peltier elements).

For our experiments, we chose to use a vertical laser beam (Fig. 1), with which it is possible to obtain more information. Indeed, the beam is first reflected from the liquid-air interface (s), then the transmitted beam crosses the fluid layer perpendicularly to the horizontal (x, y) plane, and it is reflected from the bottom of the container *(vs)*. Deflection *(vs)* is due to both the buoyancy (variation of the refraction index due to the thermal gradients within the liquid layer) and to the interface deformation, whereas deflection (s) is due only to the interface deformation [25]. From the analysis of the two beams it is possible to assess the influence of the interfacial dynamic regime as compared to what occurs both in the oil layer and at its interface. Moreover, such measurement is a non-intrusive method and the use of silicone oils (transparent oils with sufficiently high viscosities) allows large temperature gradients and measurable refraction index variations. Silicone oils are commonly used in BM experiments also because they are non-volatile liquids, have a high oxidation resistance and have an excellent thermal stability. Moreover, a more important property of silicone oils is that they have a very low surface tension and consequently silicone oil-air interfaces are not liable to any contamination that might be caused by active agents at the surface (surfactants) [3]. As it is well known, such contamination can modify thermocapillarity and therefore influences Marangoni convection [26].

The dynamics described below were observed in a small hexagonal vessel (h), filled with silicone oil (F) (Rhodorsil $47V50$ or Rhodorsil $47V20$ oils), with lateral

Table 1. Thermo-physical properties of the Rhodorsil ($47V50$ and $47V20$) silicone oils (at 25 °C).

	Thermal conductivity κ (W/mK)	Density ρ (Kg/m^3)	Kinematic viscosity ν (m^2/s)	Expansion Coefficient α (°K^{-1})	Thermal diffusivity χ (m^2/s)	Surface tension coefficient $d\sigma/dT$ (kgs^{-2} °C^{-1})	Prandtl number (Pr)
20 Cst silicone oil	0.14	0.95×10^3	2×10^{-5}	1.07×10^{-3}	0.899×10^{-7}	-2.7×10^{-5}	160
50 Cst silicone oil	0.16	0.96×10^3	5×10^{-5}	1.05×10^{-3}	0.114×10^{-6}	-2.7×10^{-5}	440

walls made of polycarbonate and a reflective polished bottom plate made of copper. The fluctuations of the temperatures imposed on this plate were about +/–0.1 °C thanks to a controlled electric heater (E)(Peltier elements). The heating rate was 0.3 °C/mn. The various gradual increases of the temperature difference were followed by the measurements at constant values of $\Delta T(Ma)$ which are maintained for periods of time longer than the largest horizontal diffusion time, $t_h = 4\Gamma^2 t_v \approx 10$ h, where t_v is vertical diffusion time, that is given by $t_v = d^2/\chi$, which is a function of the experimental conditions and varies from 561 s for $\Gamma_2 = 2.8$ and the 50 Cst silicone oil to 1112 seconds for $\Gamma_1 = 2.2$ and the 20 Cst silicone oil. Before starting the experiments, the possibility of non-uniformity in the surface temperature of the bottom plate was checked by means of infrared thermography and no horizontal temperature gradients were detected at the precision of the infrared camera (0.1 °C).

The hexagonal vessel was surrounded by the same silicone oil which was limited laterally by the cylindrical container (C) made of Perspex (diameter = 0.1 m) (Fig. 1). Due to the fact that polycarbonate has a low thermal conductivity ($\kappa_p = 0.185$ W/mK) close to that of silicone oils ($\kappa = 0.16$ W/mK for the Rhodorsil $47V50$ oil or $\kappa = 0.14$ W/mK for the Rhodorsil $47V20$ oil) and to the existence of the oil guard ring, the hexagonal vessel lateral walls can be considered as thermally insulating. The thermo-physical properties of the silicone oils used in this work, namely the Rhodorsil $47V50$ and Rhodorsil $47V20$, are given in Table 1. The temperatures at the free surface and on the copper bottom plate were measured by means of thermocouples (diameter = 0.1 mm). The uncertainty of the applied difference in temperature (ΔT) was estimated to be +/–0.1 °C. The depth (d) of the liquid layer was measured using a micrometer (precision +/–0.01 mm).

Some authors used for their experiments a thin air layer bounded from above by a sapphire plate [27] or a glass plate [28]. These plates are cooled by either air or water at a regulated temperature. In such conditions the air layer can be considered as motionless but, in such an experimental set-up, the laser beam crosses various media having various indexes of refraction. This leads to various unwanted reflected beams on the screen (S) and beam deflections which are not linked to the flow dynamics in the oil layer. Moreover, the reflected laser beams also have to cross a certain distance of air in order to obtain beam deflections that can be detected on the screen (S). For our experiments, in order to prevent the problems mentioned above, the free oil surface is in contact with air which is not bounded from above by a plate but is contained in a temperature regulated box (B) as shown in Figure 1.

Indeed, in order to reduce the possible effect of air on flow dynamics and to prevent any pollution, a small box ($0.2 \times 0.2 \times 0.2$ m^3), made of acrylic glass was used to enclose the experimental set-up (Fig. 1). The temperature of the air in the box was controlled thanks to a heat exchanger which was regulated at +/–0.5 °C. Moreover, in order to prevent temperature gradients in the box (and therefore the possible occurrence of convection in the air), the circular container (C) was surrounded by a thick annular thermally-insulating plate (A) made of Teflon which limited the heating of air from below.

Despite all these precautions, it was necessary to know the effect of air motion on flow dynamics. Any air motion in the box could have two possible effects on flow dynamics and consequently the corresponding beam deflections ((s) and *(vs)* signals) which needed to be studied.

i) First it was necessary to know the effect of any possible air motion on the (s) and *(vs)* deflections when the laser beam crosses the air layer. We studied this effect by replacing the oil layer by a mirror made of glass and having a thickness similar to that of the liquid layer. We checked that beam deflections which were due to air only were very small (<1%) and could be disregarded when compared to the deflections detected in the oil layer.

ii) The second possible effect of the air is its influence on the surface tension at the oil-air interface and thus on the deflections of the (s) and *(vs)* beams. According to Ozen et al. [29], the effect of the motion of air, which is a gas with low viscosity and low thermal conductivity, on thermocapillarity is disregarded and consequently its influence on (s) beam deflections can also be disregarded. As for the possible influence of air motion on the deflections of the *(vs)* signal (which as mentioned above contains the effects of both volume and surface tension (interface deformation)), our experiments were carried out with thick oil layers ($d = 0.8$ or 1 cm) for which buoyancy effects are much more significant than thermocapillarity. Indeed, the relative importance of surface tension and buoyancy forces is characterized by the Bond number *($Bo = Ra/Ma$)*. For our experiments, the values of Bo are high ($Bo = 24$ for $d = 0.8$ cm ($\Gamma = 2.8$) and $Bo = 37.5$ for $d = 1$ cm ($\Gamma = 2.2$)) and therefore the buoyancy effects (i.e. v: volume component in the *(vs)* signal) are dominant as compared

to thermocapillarity (i.e. s: surface component in the *(vs)* signal). Consequently, the very small effect of air on thermocapillarity (i.e. the (s) signal) is even smaller on the *(vs)* signal.

Thus, it can be concluded that the effect of air motion in the box on flow dynamics and consequently on the measured beam deflections, although it does exist, is sufficiently small in our experimental conditions for it to be disregarded.

The dynamic behaviour of the system also depends on the spatial convective pattern [7,23,24]. The relationship between spatial patterns and dynamic regimes in small aspect ratios has been studied in RB experiments [12,30]. For our experiments, in order to link the dynamic regime to the corresponding spatial pattern and thus study the interaction between spatial and temporal modes, pictures were taken simultaneously with the acquisition of the signals for each considered state. The structure was visualized by seeding the silicone oil layer with aluminium flakes.

The dynamic behaviour of the system was studied as a function of the Marangoni number (from 148 to 3636), Prandtl number ($Pr_1 = 440$ for the 50 cst. Silicone oil at 25 °C, $Pr_2 = 160$ for the 20 cst. Silicone oil at 25 °C) and the aspect ratio ($\Gamma_1 = 2.2$ ($d_1 = 1$ cm), $\Gamma_2 = 2.8$ ($d_2 = 0.8$ cm)).

2.2 Data processing techniques

As mentioned above, during the experiments two laser spots were observed on the screen (S) (Fig. 1). The first spot was obtained by reflection of the laser beam at the container bottom and contains both the volume (v) and surface (s) effects (spot *(vs)*), whereas the second corresponds to the reflection at the oil-air interface (spot (s)). The displacements of the two spots were measured and recorded by a CCD camera and a computer. The positions of the spot centres were calculated in real time using contour extraction software developed by ourselves. Thus, for each spot, its position is known from the Cartesian coordinates (x, y) with respect to an arbitrarily fixed point or from the polar coordinates (ρ, θ), the referential axis for angle calculation being horizontal. As we were interested in studying the two spots, the method used in [23,24] was not suitable for our purposes. These authors used a photodiode system which allows the measuring of the variation of luminous intensity due to the variation of the spot position. The existence of two spots required the use of specific image processing software. With the software which was developed it was possible to obtain both the magnitude and the direction of the deflection.

The time series recorded were then used to recognize and characterize the dynamic regimes, by means of spectral methods and attractor dimension calculations. Using the four signals (x_{vs}, y_{vs}), (x_s, y_s), (ρ_{vs}, ρ_s) and (θ_{vs}, θ_s), we can obtain for each signal: 1/ its Fourier spectrum, 2/ the auto-correlation function, 3/ the corresponding attractor, and 4/ its correlation dimension.

3 Analysis methods

3.1 Spectral methods

As is well known, the distinction between periodic and chaotic regimes can be made by using the power spectrum of a dynamic variable, which in our case is the laser beam deflection. In a periodic regime (i.e. a non-chaotic regime) the power spectrum of the dynamic variable displays sharp peaks at the fundamental frequencies. On the other hand, in a temporally chaotic state the power spectrum is continuous and does not show any sharp peaks. In order to validate our Fourier spectrum calculation software, mono-, bi- and tri-periodic functions were generated. The spectra obtained display the frequencies imposed when the time series were constructed.

3.2 Characterization by attractors

As the use of attractors to characterize dynamic regimes is well known nowadays, we will restrict ourselves here to describing the overall concept. By examining only one single dynamic variable $x(t)$ it is possible to determine the entire orbit in the phase space and the construction of the corresponding attractor. The method used is the well-known reconstruction technique (Takens [31,32] and Packard et al. [33]) which is briefly described below. The attractor was constructed in a phase space of (n) dimensions. For this purpose, (n) values of the variable (x) were taken: ($x(t)$, $x(t+t_d)$, ... $x(t+(n-1)t_d)$; t_d is the time delay, which is a multiple of the sampling period Δt, $t_d = p\Delta t$, where (p) is an integer.

Strange attractors corresponding to chaotic systems are typically characterized by a fractal dimension (D) smaller than the degrees of freedom of the system. The correlation dimension of Grassberger and Procaccia [34,35] is one of many ways to define the dimension of an attractor and it is the most commonly used, particularly in the characterization of the experimental time series.

The attractor correlation dimension was calculated from a locally measured time series by the method proposed by Grassberger and Procaccia [34,35]. (D) is estimated by the exponent which is given by the asymptotic behaviour r^D of the integral correlation function $C(r, N)$:

$$C(r, N) = \frac{1}{N^2} \sum_{i,j=1 i \neq j}^{N} H\left(r - |X_i - X_j|\right) \qquad (1)$$

where N is the total number of points, $H()$ is the Heaviside function and (X_i) is a vector in the $n - D$ phase space obtained from the reconstructed time series using the time delay (t_d) and the reconstruction technique described above. In practice, the correlation integral is evaluated using reference points. The averaged numbers of points in hyper-spheres centered on the reference points with radius (r) were calculated to evaluate the above equation. $C(r)$ was determined using 18 000 to 250 000 data

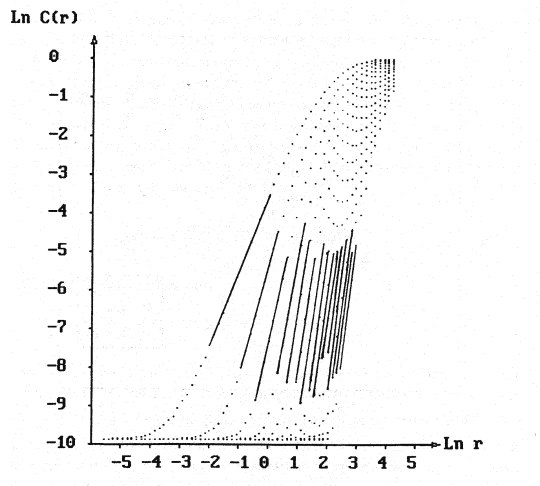

Fig. 2. The integral correlation function for various dimensions (n) of the phase space ($Ln - Ln$ plot). (n) varies from 2 to 16 (from left to right); the slopes of linear regions give the correlation dimension (D).

points in order to meet the *Tsonis* criterion which considers (N) required for reliable calculations of the correlation dimension (D) to be exponentially linked to the correlation dimension (that is $N \sim 10^{2+0.4D}$). A maximum dimension of the phase space equal to 16 and 100 reference points were used [36–38].

To avoid the correlations between the reference points, these points were chosen as follows: the time series were divided into 100 intervals, and the first point of each interval was chosen as a reference point. The number of radii was equal to 100 and the smallest radius was taken as being equal to the smallest distance between two points of the attractor. The radius step (Δr) was chosen as the nth root of 2, most often $\sqrt[4]{2}$ [36–38]. In order to count the number of points in the hyper-spheres, it is necessary to calculate the distances between the various points and the reference points. The rapidity of these calculations depends on the norm chosen. The first norm was chosen, as in [36–38], because it is the norm which allows quick calculations.

The slope in the $Ln - Ln$ plot of $C(r)$ was calculated using the least square method in the linear parts of the curves (Fig. 2). The calculations were carried out by increasing the embedding dimension of the phase space until the convergence of the correlation dimension (D) is achieved. Thanks to a preliminary study, we reached the conclusion that the value of (p) (which is involved in the reconstruction method) does not affect the convergence of the calculation of the attractor dimension. (p) was taken as being equal to 2.

Software was developed which allows the calculation of the correlation dimension as described above. It was validated by using periodic functions (mono periodic, $D = 1$ and bi-periodic, $D = 2$) and by calculating the dimensions of Hénon's model attractor ($D = 1.22$ with $N = 20\,000$, $a = 1.4$ and $b = 0.3$) and Coullet – Feigenbaum's model attractor ($D = 0.50$ with $N = 20\,000$, $\lambda = 3.57$). The dimensions, calculated by means of our software, are in good agreement with those calculated by other authors for the same theoretical model coefficients [36,39,40].

4 Typical results

4.1 Deflections due to the temperature field and the free surface deformation

When a laser beam crosses an isothermal layer of a transparent liquid with a flat free surface, this beam is reflected at the bottom ($z = 0$) and its spot, which is observed on a screen, has a uniform brightness b_0. In a convective state, the temperature field $T(x, y, z)$ and the deformation of the free surface $h(x, y)$ induce laser beam deflection. This deflection leads to a variation $\delta b(x, y)$ of spot brightness from homogeneous distribution. We report here the approach of Thess and Orszag [41] in order to estimate respectively the deflection due to the temperature field:

$$\left(\frac{\delta b}{b_0}\right)_T = 2H\left(\frac{dn_0}{dT}\right)\left(\partial_x^2 + \partial_y^2\right)\int_{z=0}^{z=d} T(x, y, z)dz \qquad (2)$$

and that due to the free surface deformation:

$$\left(\frac{\delta b}{b_0}\right)_h = -H(2n_0 - 1)\left(\partial_x^2 + \partial_y^2\right)h(x, y) \qquad (3)$$

where n_0 is the liquid index of refraction at $T = T_0$ and dn_0/dT is the coefficient of its variation with temperature. For silicone oils, $n_0 \approx 1.4$ and $dn_0/dT \approx -10^{-4}K^{-1}$. ($H$) is the distance between the screen and the free surface and (d) the liquid layer depth. Consequently, if the deformation $h(x, y)$ and the temperature field $T(x, y, z)$ are known, the relative importance of volume and interface deformation effects on the laser beam deflection (the variation of brightness being equivalent to the magnitude of beam deflection) can be estimated.

According to [42],

$$T(x, y, z) = T_i - (T_i - T_s)\frac{z}{d} + (T_i - T_s)\theta(z)f(x, y) \qquad (4)$$

the polynomial function $\theta(z)$ is estimated as in [42]:

$$\theta\left(\frac{z}{d}\right) = 0.6\left(\frac{z}{d}\right) + 0.015\left(\frac{z}{d}\right)^2 + 0.12\left(\frac{z}{d}\right)^3 \qquad (5)$$

and according to [43],

$$h(x, y) = H_0 f(x, y) \qquad (6)$$

with $H_0 \approx 10^{-3}$ mm [43], which leads to:

$$r = \frac{\left(\frac{\delta b}{b_0}\right)_T}{\left(\frac{\delta b}{b_0}\right)_h} = 0.036.d.(T_i - T_s) \qquad (7)$$

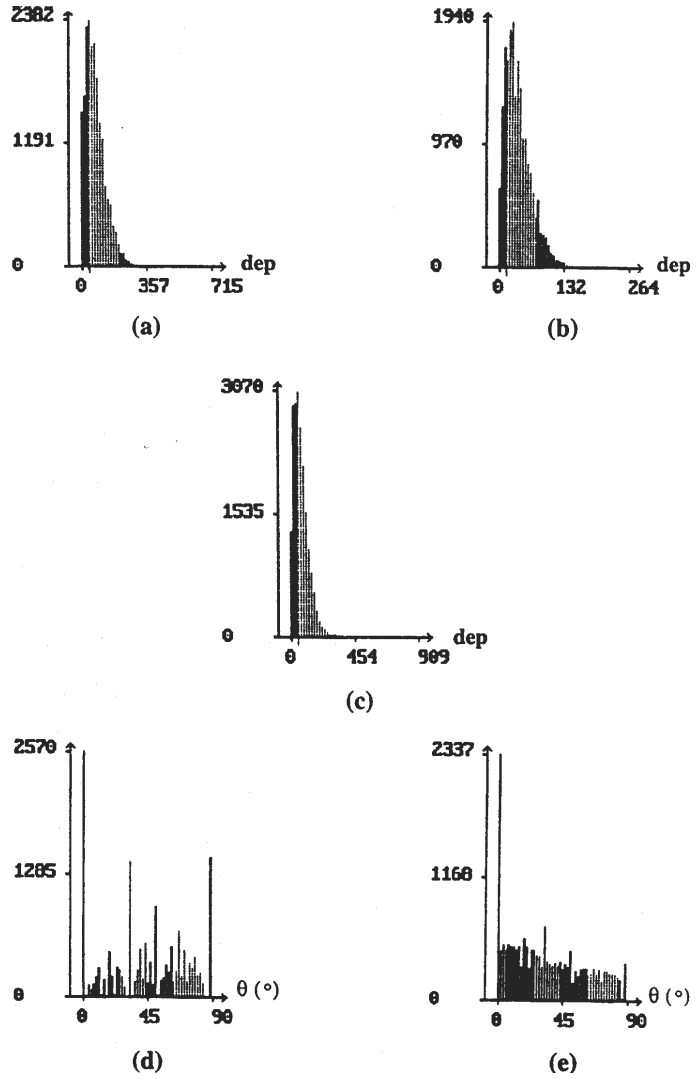

Fig. 3. Displacement histograms. $\Gamma_1 = 2.2$, $Pr_1 = 440$. Displacement magnitudes: (a) spot (s), $Ma = 355$. (b) spot *(vs)*, $Ma = 355$. (c) spot *(vs)*, $Ma = 958$. Displacement angles: (d) spot (s), $Ma = 247$. (e) spot (s), $Ma = 1,135$.

with d: depth of the liquid layer (mm), T_i: temperature of the lower limiting surface, T_s: temperature of the upper limiting surface.

In our case, (r) varies from 1.1 to 8.3 for a (ΔT) increased from 3 °C to 23 °C for $d_1 = 1$ cm, and from 1.2 to 6.9 for a (ΔT) increased from 4 °C to 24 °C for $d_2 = 0.8$ cm. Thanks to these calculations, it can be concluded that the deflection due to temperature field variation is always greater than that corresponding to free surface deformation.

In Figure 3 the displacement magnitude and angle histograms of the spots *(vs)* and (s) are shown. From Figures 3a, 3b and 3c, it can be noted that: i) for the same $Ma(= 355)$ larger displacements of spot (s) are observed than for the spot *(vs)*; ii) there are more small displacements in the histogram of spot (s) (Fig. 3a) than for the *(vs)* histogram (Fig. 3b); iii) the more complex the system (increased Ma), the smaller the displacements are (Figs. 3b and 3c). In the angle histograms (Figs. 3d and 3e), it can be noted that there are some preferred directions for the displacements. Indeed, peaks are observed around the 0°, 30°, 45° and 90° angles. On the other hand, when the system becomes more complex (increased Ma) the histogram tends to become more uniform (Fig. 3e).

In Figure 4, the average displacements of spots *(vs)* and (s) versus *(Ma)* for various Pr and Γ are shown. It can be noted that: i) the displacement increases with *(Ma)* for all experimental conditions; ii) for the same Pr $(Pr_2 = 160)$ and $\Gamma_1 = 2.2$, *(vs)* displacements are larger than those of the spot (s), which agrees with the conclusion of the calculations mentioned above; iii) for the same aspect ratio $(\Gamma_1 = 2.2)$ and a fixed value of *(Ma)*, the average value of the *(vs)* displacement is greater at higher Pr $(Pr_1 = 440)$ than at the lower one $(Pr_2 = 160)$.

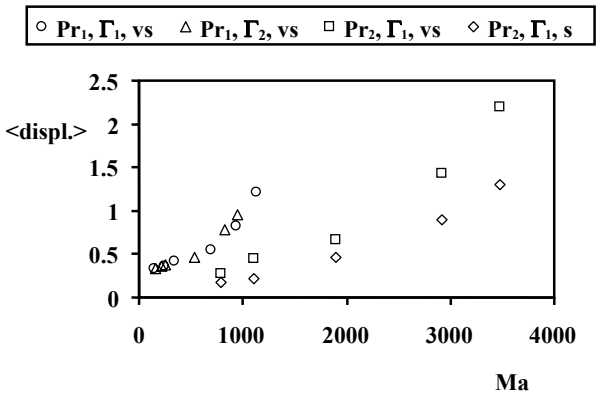

Fig. 4. Average displacements of the spots (s) and (vs), for various Ma, Pr and Γ.

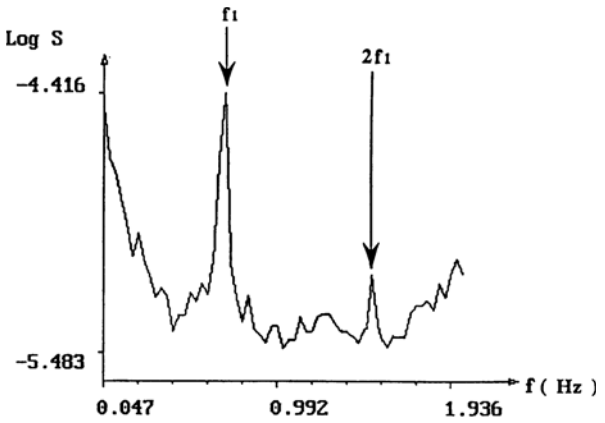

Fig. 5. Fourier spectrums of the (vs) signal. Mono-periodic regime. The fundamental frequency $f_1 = 0.7$ Hz and its harmonic. $Ma = 222$; $Pr_1 = 440$ at 25 °C; $\Gamma_1 = 2.2$.

4.2 Transition to temporal chaos

As an example of a sequence of transitions between dynamic regimes leading to chaos, the experiment carried out at $Pr_1 = 440$ and $\Gamma_1 = 2.2$ is described below. The first bifurcation observed after the onset of convection is analogous to the Hopf bifurcation in RB convection, which leads to a time-dependent regime. Indeed, for $Ma = 222$, Figure 5 shows a spectrum of the *(vs)* signal with one peak at the frequency $f_1 = 0.7$ Hz and its harmonic, which corresponds to a mono-periodic regime. By increasing Ma to 370, a second peak is observed at the frequency $f_2 = 1.1$ Hz (Fig. 6), which corresponds to a bi-periodic state. All the other peaks can be analyzed as linear combinations of the two fundamental frequencies. With a further increase of Ma to 543, a chaotic state is observed, which is characterized by a continuous spectrum without any peaks (Fig. 7) and an auto-correlation function which vanishes for a long period of time (Fig. 8).

Such transition to temporal chaos, via quasi-periodicity, was also observed in RB instability. Indeed, the transition to temporal chaos via quasi-periodicity in RB convection was observed to occur either from a bi-periodic to a chaotic state, or from a tri-periodic regime to chaos [23,24]. For BM instability, the transition to temporal chaos via quasi-periodicity, for these experimental conditions ($Pr_1 = 440$ and $\Gamma_1 = 2.2$), seems to occur only via a bi-periodic regime and the destruction of a $T2$ torus.

Fig. 6. Fourier spectrum of the (vs) signal. Bi-periodic regime. $Ma = 370$; $Pr_1 = 440$ at 25 °C; $\Gamma_1 = 2.2$. $f_1 = 0.7$ Hz and $f_2 = 1.1$ Hz.

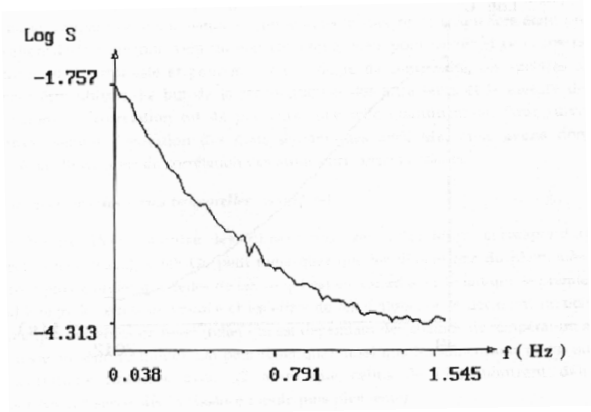

Fig. 7. Fourier spectra of the (vs) signal. Chaotic regime. $Ma = 543$; $Pr_1 = 440$ at 25 °C; $\Gamma_1 = 2.2$.

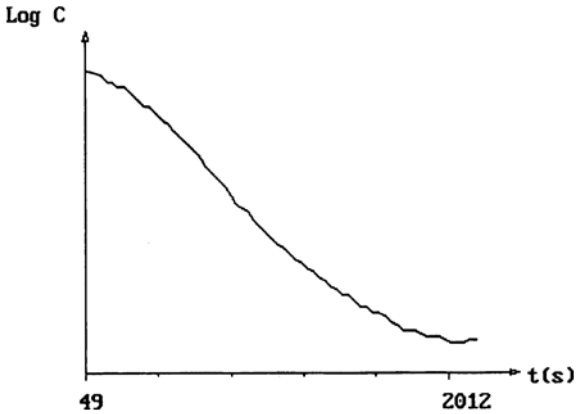

Fig. 8. Autocorrelation function of the (vs) signal. Chaotic regime. $Ma = 543$; $Pr_1 = 440$ at 25 °C; $\Gamma_1 = 2.2$.

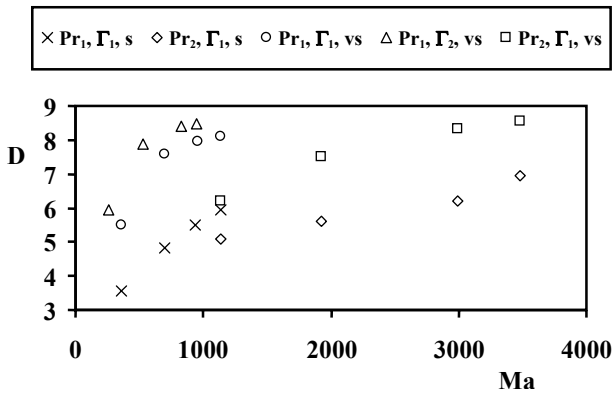

Fig. 9. Variations of the correlation dimensions of the (s) and (vs) signals as functions of Ma, Pr and Γ.

4.3 Dimensions of the strange attractors

The appearance of a broad continuous band in the Fourier spectrum is the indication of the transition to a chaotic state. However, to know if this chaos is random or deterministic and to measure the degree of strangeness, other methods need to be used. The aim of attractor construction and correlation dimension calculation is to provide such information. Thus, in order to follow, quantitatively the evolution of the chaotic dynamic regimes with the increase of *(Ma)*, the correlation dimensions of the corresponding attractors were calculated.

In Figure 9 the attractor dimensions of the *(vs)* and (s) signals are plotted as functions of *(Ma)* for various Pr and Γ. It can be noted that the *(vs)* dimensions are larger than those of (s), which is in agreement with the fact that the *(vs)* signal contains both volume and interface deformation effects whereas the (s) signal corresponds only to the free surface deformation. It can also be seen in Figure 9 that chaos develops with *(Ma)* for all experimental conditions. It is also shown that the (s) dimension increases linearly with *(Ma)*, whereas the variation of the *(vs)* dimension, as a function of *(Ma)* for fixed values of Pr and Γ is composed of two parts: at first it increases rapidly, then the increase is slower.

For $Pr_1 = 440$, the influence of the aspect ratio on the correlation dimension was considered. It can be seen that, as expected, the system is more complex for $\Gamma_2 = 2.8$ than for a smaller aspect ratio ($\Gamma_1 = 2.2$) (Fig. 9). A similar result was also reached by Libchaber and Maurer [44], who showed, for a RB experiment with helium, the large dependence of temporal behaviour as a function of the aspect ratio. They observed periodic oscillations for $\Gamma < 3$ and chaotic regimes for $\Gamma > 3$, starting from a Rayleigh number twice its critical value.

The dimension of the time series, corresponding to the distance between the two spots (i.e. spots *(vs)* and (s)), was also calculated. The dimension was found to be constant ($D = 7 \pm 0.1$), which leads us to think that this dimension might be linked to the depth of the oil layer, which is constant for all the experiments conducted with the same aspect ratio.

4.4 Transition to spatio-temporal chaos

As the dynamic regime is linked to the spatial convective pattern [7], pictures of the pattern were taken in order to try to provide answers concerning the nature of the chaos (temporal or spatio-temporal). For example, Figure 10 shows pictures corresponding to the two values of the *(Pr)* number for $\Gamma_1 = 2.2$. Thus, one convective cell is observed, for a larger range of *(Ma)* for $Pr_2 = 160$ than for $Pr_1 = 440$. Indeed, a breaking of the convective cell occurs at $Ma = 1581$ for Pr_2 and at $Ma = 740$ for Pr_1. Consequently, for the above mentioned values of *(Ma)*, transitions to spatio-temporal chaos are observed through the mobility of the pattern and the involvement of the spatial modes. The breaking of the convective cell is probably due to a very strong chaotic state which leads to the excitement and appearance of other spatial modes. For example, in RB instability the range of the Rayleigh number, for which deterministic (temporal) chaotic regimes are observed, is often limited and when the Rayleigh number is further increased the convective pattern is broken and spatial chaos is observed.

From the pictures in Figure 10 and the curves in Figure 9 it can be concluded that for $Pr_2 = 160$ and $Ma < 1581$, the chaos is temporal and (D) is around 5 for the (s) signal and slightly higher than 6 for (vs). For $Pr_1 = 440$, the chaos is spatio-temporal for $Ma > 740$ and the dimension (D) is around 8 for the (vs) signal and varies from 5 to 6 for the (s) signal.

5 Conclusions

A transition to temporal chaos via quasi-periodicity, as in RB convection, was observed in BM convection in a small aspect ratio geometry ($\Gamma = 2.2$). This transition occurs via a bi-periodic regime and the destruction of a $T2$ torus.

The calculated attractor dimensions (from 3.5 to 8.5) for BM instability are larger than those found for RB instability in similar confined geometries [20] but they are close to those found by Sato et al. [21] (6.5 or 9) in a quasi-one-dimensional RB system ($\Gamma_x = 15$ and $\Gamma_y = 1$). The BM dimensions are also of the same order as those calculated in an electro-convection system (=5.1) [45]. The difference between the values of the dimensions obtained in this work compared to those of confined RB convection (aspect ratios of the same order) can be attributed to the fact that in our experiments, in addition to the buoyancy effects, as in RB convection, surface tension effects are also involved. Therefore, it is evident that in BM convection the number of independent variables that must be specified is larger than in RB instability (the dimension of an attractor being linked to the number of independent variables required to specify a system state at any given time). As for the effect of air, although it does exist, it has been proved to be sufficiently small for our experimental conditions in comparison with buoyancy and surface tension effects to be disregarded.

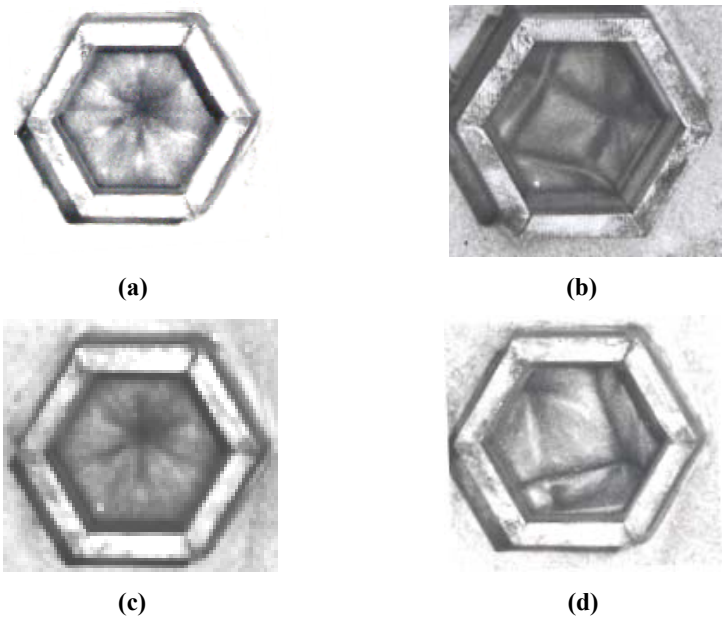

Fig. 10. Pictures of the convective patterns corresponding to various Ma and Pr. $\Gamma_1 = 2.2$. The structures in (b) and (d) are moving; the patterns shown are observed at a given time. $Pr_1 = 440$: (a) $Ma = 247$; (b) $Ma = 962$. $Pr_2 = 160$: (c) $Ma = 790$; (d) $Ma = 1928$.

It can also be concluded that chaos develops with *(Ma)* for all experimental conditions. As for the variation as a function of the aspect ratio, the system is more complex for $\Gamma = 2.8$ than for a smaller aspect ratio ($\Gamma = 2.2$).

The transition from temporal chaos to spatio-temporal chaos has also been observed. For larger values of the Marangoni number, spatial modes are involved through pattern dynamics. For $\Gamma = 2.2$, at $Pr_2 = 160$ and $Ma < 1581$, the chaos is temporal and (D) is around 5 for the (s) signal and slightly higher than 6 for (vs). For $Pr_1 = 440$, the chaos is spatio-temporal at $Ma > 740$ and the dimension (D) is around 8 for the (vs) signal and varies from 5 to 6 for the (s) signal.

This work will be continued in the future by carrying out other studies in order to know if other scenarios (intermittency, sub-harmonic cascade) may also lead to a chaotic regime in BM convection. With the correlation dimension it is possible to obtain general information about the degree of strangeness of the system and about the average rate of its trajectory divergence. However, the correlation dimension does not make possible to know whether there are one or more dilatant directions on the attractor and does not therefore allow the consideration of the other property of the strange attractors, that is their sensivity to initial conditions. Lyapunov exponents [46,47] allow the obtaining of such information because they give information about the local stability properties of the attractor. Thus, this study will be pursued using Lyapunov exponents in order to confirm the results obtained in this work and to go deeper into the characterization of the attractors.

References

1. M.C. Cross, P.E. Hohenberg, Rev. Mod. Phys. **65**, 851 (1993)
2. E. Bodenschatz, W. Pesch, G. Ahlers, Ann. Rev. Fluid Mech. **32**, 709 (2000)
3. M.F. Schatz, G.P. Neitzel, Ann. Rev. Fluid Mech. **33(6)**, 93 (2001)
4. E.A. Ramadan, J.M. Hay, R.E. Khayat, J. Non-Newtonian Fluid Mech. **115**, 79 (2003)
5. F.T. Akyildiz, H. Bellout, Applied Mathematics and Computation **162**, 1103 (2005)
6. M. Bestehorn, Phys. Rev. E **48**, 3622 (1993)
7. F. Sain, H. Riecke, Physica D **144**, 124 (2000)
8. W.V.R. Malkus, Proc. Roy. Soc. A **225**, 196 (1954)
9. G.E. Willis, J.W. Deardorff, Phys. Fluids **10**, 931 (1967)
10. R. Krishnamurti, J. Fluid Mech. **42**, 309 (1970)
11. G. Ahlers G., Phys. Rev. Lett. 33, 1185 (1974)
12. J.P. Gollub, S.V. Benson, J. Fluid Mech. **100**, 449 (1980)
13. J.P. Gollub, S.V. Benson, J. Steinman, in *Nonlinear Dynamics*, edited by R.H.G. Helleman (Annals of the New York Academy of Sciences, 1980), Vol. 357, p. 22
14. M. Giglio, S. Musazzi, U. Perini, Phys. Rev. Lett. **47**, 243 (1981)
15. A. Libchaber, J. Maurer, J. Phys. Colloq. France **41**, C3-51 (1980)
16. A. Libchaber, C. Laroche, S. Fauve, J. Phys. Lett. **43**, 211 (1982)
17. P. Bergé, M. Dubois, P. Manneville, Y. Pomeau, J. Phys. Lett. **41**, L 341 (1980)
18. M. Dubois, M.A. Rubio, P. Bergé, Phys. Rev. Lett. **51**, 1446 (1983)
19. M. Sano, Y. Sawada, *Chaos and Statistical Methods*, edited by Y. Kuramoto (Springer-Verlag, Berlin, 1984)

20. M. Dubois, P. Bergé, Physica Scripta **33**, 159 (1986)
21. S. Sato, M. Sano, Y. Sawada, Phys. Rev. A **37**, 1679 (1988)
22. T. Boeck, N.K. Vitanov, Phys. Rev. E **65**, 3720 (2002)
23. P. Bergé, Y. Pomeau, C. Vidal, *Order within Chaos* (Wiley, New York, 1984)
24. P. Bergé, *Le Chaos: théorie et expériences* (Eyrolles, 1988)
25. P. Cerisier, C. Jamond, J. Pantaloni, J.C. Charmet, J. Phys. France **45**, 405 (1984)
26. J.C. Berg, A. Acrivos, Chemical Engineering Science **20**, 737(1965)
27. M.F. Schatz, S.J. VanHook, W.D. McCormick, J.B. Swift, H.L. Swinney, Phys. Fluids **11**, 2577 (1999)
28. P. Cerisier, S. Rahal, B. Billia, Phys. Rev. E **54**, 3508 (1996)
29. O. Ozen, E. Theisen, D.T. Johnson, P.C. Dauby, R. Narayanan, Journal of Colloid and Interface Science **289**, 271 (2005)
30. M. Dubois, P. Bergé, Phys. Lett. **93**, 365 (1983)
31. F. Takens, in *Dynamical Systems and Turbulence*, edited by D.A. Rand, L.S. Young (Springer-Verlag, Berlin, 1981)
32. F. Takens, in *Dynamical Systems and Bifurcations,* edited by H.W. Broer, F. Takens (Springer-Verlag, New York, 1985)
33. N.H. Packard, J.P. Crutchfield, J.D. Farmer, R.S. Shaw, Phys. Rev. Lett. **45**, 712 (1980)
34. P. Grassberger, I. Procaccia, Phys. Rev. Lett. **50**, 346 (1983)
35. P. Grassberger, I. Procaccia, Physica D **9**, 189 (1983)
36. C. Lausberg, Ph.D. thesis, INPG, Grenoble, France, 1987
37. H. Abarbanel, R. Brown, J.J. Sidorowich, L.S. Tsimiring, Rev. Mod. Phys. **65**, 1331 (1993)
38. J.C. Sprott, Chaos and Time-Series Analysis (Oxford University Press, 2003)
39. P. Cvitanovic, G. Gunaratne, I. Procaccia, Phys. Rev. A **38**, 1503 (1988)
40. S. Chang, J. McCown, Phys. Rev. A **30**, 1149 (1984)
41. A. Thess, S.A. Orszag, J. Fluid Mech. **283**, 201 (1995)
42. P. Cerisier, R. Occelli, J. Pantaloni, Physico-Chemical Hydrodynamics **7(4)**, 191 (1986)
43. C. Perez-Garcia, J. Pantaloni, R. Occelli, P. Cerisier, J. Phys. France **46**, 2047 (1985)
44. A. Libchaber, J. Maurer, J. Phys. Lett. France **39**, L 369 (1978)
45. B. Malraison, P. Atten, P. Bergé, M. Dubois, C.R. Acad. Sc. Paris **297**, 209 (1983)
46. J.P. Eckmann, S. Oliffson - Kamphorst, D. Ruelle, S. Ciliberto, Phys. Rev. A **34**, 4971 (1986)
47. F.E. Udwadia, H.F. Von Bremen, Appl. Math. Comput. **121**, 219 (2001)